Solid State Reduction Driven Synthesis of Mn Containing Multi-principal Component Alloys



WOOKYUNG JIN, PRINCE SHARMA, PRASHANT SINGH, ANIMESH KUNDU, GANESH BALASUBRAMANIAN, and HELEN M. CHAN

In recent years, high entropy alloys (HEAs), also known as multi-principal component alloys (MPCAs) have emerged as a new and exciting class of materials. This paper reports on the solid state reduction synthesis of a series of CoFeNiMn-based MPCA compositions, starting from a mixture of the corresponding oxides. One of the aims of the study was to test whether the degree of reduction of MnO, a highly stable oxide, could be enhanced by tailoring the alloy composition. Specifically, the influence of Ni content was studied because Ni exhibits a significant negative enthalpy of mixing with Mn. High purity precursor powders of Co(OH)₂, Fe₂O₃, MnO₂, and NiO were milled and mixed using standard ceramic processing methods. The nominal sample compositions (assuming complete oxide reduction) were (CoFeMn)_xNi_(1-x), for x = 0, 0.083, 0.166, and 0.25. The oxide samples were subjected to a series of isothermal reduction anneals in flowing 3 pct H₂-Ar at 1100 °C. The resulting microstructures were characterized using scanning electron microscopy (SEM), X-ray energy dispersive spectroscopy (EDS) and X-ray diffraction (XRD). The composition of the resulting MPCAs was determined quantitatively using wavelength dispersive spectroscopy (WDS) in the electron microprobe. The study revealed that for each of the initial oxide compositions studied, it was possible to achieve an MPCA with ~ 25 at. pct Mn. These results were found to be consistent with the predictions of a thermodynamic model whereby a negative enthalpy of mixing (ΔH_{mix}) , combined with a contribution from configurational entropy, can offset a positive free energy of reduction (ΔG_{red}). The incorporation of vibrational entropy into first principles calculations was found to have a significant effect on the predicted crystal structure of the MPCAs.

https://doi.org/10.1007/s11661-024-07490-w © The Minerals, Metals & Materials Society and ASM International 2024

I. INTRODUCTION

MULTI-PRINCIPAL component alloys (MPCAs) are a new class of materials which unlike conventional alloys, comprise multiple principal components in equimolar or near equimolar ratios. [1-11] The stabilization of certain crystallographic phases in these systems has been attributed to the increased configurational entropy, hence their original designation as high entropy alloys (HEAs). This concept has opened an expansive realm of unexplored alloy compositions and

microstructures, and has attracted significant research interest. The excitement in the field has been fueled by the discovery that select MPCA compositions exhibit properties that are superior to conventional alloys. For example, the Cantor alloy (and related compositions) have been shown to exhibit exceptional mechanical properties, [12,13] especially at low temperatures. [14,15] Also, several refractory MPCAs have been identified that retain higher strengths at elevated temperatures compared to conventional superalloys, *e.g.* Senkov *et al.* [16] showed that V₂₀Nb₂₀Mo₂₀Ta₂₀W₂₀ outperforms Inconel 718 and Haynes 230, retaining high strength up to 1600 °C. Notably, the vast majority of MPCAs have been synthesized by melt processes (such as arc-melting and induction melting)^[7–9] and laser deposition additive manufacturing (AM) techniques. [17–21]

For many elemental metals (e.g. Fe, Sn, Cu, Cr), the reduction of simple oxides has been widely studied, and is a long-established route by which they are extracted from their ores, usually in the molten state.^[22,23] The synthesis of a few binary alloys by solid state reduction has been previously investigated, [24-27] usually with the aim of achieving a specific sample geometry. For

METALLURGICAL AND MATERIALS TRANSACTIONS A

WOOKYUNG JIN and HELEN M. CHAN are with the Department of Materials Science & Engineering, Lehigh University, Bethlehem, PA 18015. Contact e-mail: hmc0@lehigh.edu PRINCE SHARMA, ANIMESH KUNDU, and GANESH BALASUBRAMANIAN are with the Department of Mechanical Engineering & Mechanics, Lehigh University, Bethlehem, PA 18015. PRASHANT SINGH is with the Ames National Laboratory of US Department of Energy, Iowa State University, Ames, IA 50011. Manuscript submitted February 29, 2024; accepted June 13, 2024. Article published online July 2, 2024

instance, Nadler et al.^[24] report the fabrication of Fe–Cr honeycombs by reduction of an extruded mixture of iron oxide and chromium oxide, while Verdooren and co-workers describe the fabrication of Fe₂O₃ ceramic foam precursors that are subsequently reduced to closed metallic foam bodies.^[28,29] To the authors' knowledge, however, the only reports of applying this reduction technique to the synthesis of an MPCA are the studies by the Dunand group^[30] and Koube et al.^[31]; both studies addressed a possible method for AM of HEAs. These papers describe 3D extrusion of polymeric inks containing a blend of oxide powders, followed by co-reduction in a pure hydrogen atmosphere.

Recent efforts from the Lehigh group have demonstrated that by using a dilute H2 gas environment, MPCAs can be synthesized via the solid state reduction of an oxide powder mixture. [32,33] For convenience, we have designated this technique as RedSSOx—reduction of solid state oxides. Compared to melt-processing, advantages of RedSSOx include lower operating temperatures and improved compositional homogeneity, since segregation during solidification is no longer an issue. The initial work of Gianelle et al. demonstrated the feasibility of fabricating bulk samples of the MPCA CoCuFeNi by reduction of a pressed pellet of the constituent oxides (Co₃O₄, CuO, Fe₂O₃ and NiO).^[32] The synthesis was performed in the solid state using 5 pct H₂-N₂ as the reduction atmosphere (note that the use of forming gas is experimentally convenient since the H₂ content is below the flammability limit.) Complete reduction of the (initially) ceramic samples was achieved, resulting in a microstructure consisting of two metallic FCC phases, a polycrystalline matrix and an intergranular Cu-rich phase. In a subsequent study, the RedSSOx process was extended to the Cantor alloy composition CoCrFeNiMn, hence incorporating alloying elements such as Cr and Mn, the oxides of which are thermodynamically much more stable than those of Cu, Fe, Ni and Co. [33] In order to prevent the formation of nitrides, reduction was carried out in a 3 pct H₂-Ar atmosphere. A reduction heat treatment at 1185 °C for 120 hours resulted in the formation of a core-shell sample, with an outer layer comprising a metallic alloy. The composition of the alloy was determined quantitatively using electron microprobe analysis as Co_{0.25}Cr_{0.19}-Fe_{0.25}Ni_{0.23}Mn_{0.08} (at. pct). Although this composition differed from that of the targeted equiatomic Cantor alloy, nonetheless the result demonstrated the successful reduction of the chromium and manganese oxides.

The reduction to metallic Mn was unexpected, and the authors proposed a model to rationalize their findings. [33] The postulate was that the enhanced reduction results from an additional contribution to the total free energy change due to a *negative enthalpy of mixing* ($\Delta H_{\rm mix}$). In principle, therefore, the reduction of a given oxide (MO) would be favored, if metal M exhibits a negative enthalpy of mixing with the other alloying elements, *i.e.* providing its formation of a *solid solution* is thermodynamically favored. The goals of the current study were several fold. Firstly, since only 8 at. pct Mn was achieved in our prior study, one goal was to demonstrate the successful RedSSOx synthesis of an

MPCA with a significant (> 20 at. pct) Mn concentration. A second goal was to test the solid solution model by studying a series of compositions with differing values of $\Delta H_{\rm mix}$, and comparing the reduction behavior.

In order to build on previous results, the same Cantor related family of elements was considered (Fe, Co, Ni, Mn, Cr). Of the corresponding oxides, Cr₂O₃ and MnO are the most stable and unlike CoO, NiO and FeO, cannot be reduced using dilute hydrogen mixtures. To facilitate analysis and interpretation of the results, Cr₂O₃ was omitted, and the present work focuses on the reducibility of MnO. It is worth noting that the reduction of manganese(IV) oxide (MnO₂) is a complex process, whereby a series of intermediate oxides is formed with progressively lower oxygen content: MnO₂ \rightarrow Mn₂O₃ \rightarrow Mn₃O₄ \rightarrow MnO \rightarrow Mn. [34] Whereas reduction from MnO₂ to MnO can be achieved relatively easily at pO₂ values $\sim 10^{-4}$, [35] MnO is very stable. There is the general recognition that reduction of MnO to Mn is not achievable at temperatures below the melting point of Mn, using either hydrogen or CO gas mixtures.[36-38]

Ideally, we would wish to test the solid solution model by first evaluating $\Delta H_{\rm mix}$ for a continuous range of compositions within the Co-Fe-Ni-Mn alloy system. Unfortunately, this data is not readily available. Firstly, reports of experimental measurements are limited, and mostly restricted to selected binary systems. The alternative route, calculating values of ΔH_{mix} from first principles is feasible, but far from straightforward. One of the most challenging issues is the appropriate incorporation of contributions due to vibrational entropy. Our preliminary studies revealed that if vibrational entropic effects were ignored, the enthalpy calculations provided guidance on the influence of compositional trends, but there were inconsistencies between the calculated values and experimental observations. Disparities also existed between the predicted and observed crystal structures (HCP versus FCC) for the compositions of interest. We believe that the root of these inconsistencies lies in the neglect of considerations of vibrational entropy. Despite the challenges this problem presents, we are pursuing an approach to carry out such computations (see Section II-B-1), and this work is currently ongoing. As a first step, however, the decision was taken to focus on the role of vibrational entropies in determining the relative stability of the different crystal structures for the metallic MPCAs.

For the aforementioned reasons, the $\Delta H_{\rm mix}$ values utilized in this work were derived from binary data using the Miedema mixing model. [39,40] The corresponding binary enthalpy of mixing values for (equimolar) Co–Mn, Fe–Mn and Ni–Mn are depicted in Table I⁽³⁹⁾; it can be seen that the alloying element that exhibits the most negative enthalpy of mixing with Mn is *nickel*, where $\Delta H_{\rm mix}$ of Ni–Mn is ~ -8 kJ/mol. Based on this information, it was decided to investigate the effect of increasing Ni content on the processing of Co–Fe–Ni–Mn MPCAs *via* oxide reduction. Specifically, a series of alloys with target nominal compositions (assuming 100 pct reduction) (CoFeMn)_{1-x}Ni_x were investigated, where $0 \leq x \leq 0.25$ (at. pct). It can be seen

Table I. Values of ΔH_{mix} [AB] (kJ/mol) Calculated by Miedema's Model for Atomic Pairs^[39]

$\Delta H_{\text{mix}}[AB]$ (kJ/mol)	Co	Cr	Fe	Mn	Ni
Co Cr Fe Mn		- 4	- 1 - 1	- 5 2 0	0 - 7 - 2 - 8

that the elements Co-Fe-Mn can be considered as a group, where the initial mole fractions of the oxides of Co, Fe and Mn are equal, regardless of Ni content.

II. METHODS

A. Experimental

1. Sample processing

The following commercially available high purity oxide powders were used for this study: Co(OH)₂ (99.9 pct), MnO₂ (99.9 pct), NiO (99.998 pct) (Fisher Scientific), and nano-Fe₂O₃ (Sigma-Aldrich Inc). Different batches of oxide powder mixtures were prepared corresponding to the following targeted metallic compositions (assuming complete reduction), (CoFeMn)_{1-x} Ni_x , where x = 0, 0.083, 0.166, and 0.250. The powders were wet-milled for ~ 6 hours in iso-propanol using high purity alumina balls (diameter ~ 5 mm). Reference samples consisting solely of MnO₂ were also prepared. After milling, the powder mixtures were sieved to separate the milling media, washed and dried under vacuum. Cylindrical pellets ($\sim 12.7 \times 7 \text{ mm}^2$) were prepared by uniaxial pressing in a steel die under a pressure of ~ 176 MPa for 5 minutes. The pressed pellets were subsequently packed in a graphite crucible with graphite powder and subjected to isothermal reduction heat treatment for varying times at 1100 °C under a flowing 3 pct H₂-Ar atmosphere. The heating and cooling rate of the tube furnace (GSL-500x) was 5 °C/min. Note that the 3 pct H₂-Ar mixture was used rather than forming gas (5 pct H₂-N₂) to circumvent the formation of nitrides. Like forming gas however, it is experimentally convenient as the hydrogen content is below the flammability limit.

2. Materials characterization

Following the reduction heat-treatment, the specimens were sectioned and mounted in epoxy. In each case, damage from the cutting process was eliminated by successively grinding with finer grit SiC papers such that a surface layer of ~ 0.5 mm was removed. Next, the samples were polished using a sequence of successively finer diamond suspensions (6, 3, 1 and 0.05 μ m). Scanning electron microscopy (Hitachi S-4300, 10 kV) was used to characterize the microstructure of the samples. Elemental mapping was carried out using energy dispersive X-ray spectroscopy (EDS, EDAX Octane SDD, 20 kV). Quantitative elemental analysis of the phases present was performed using WDS

(wavelength dispersive spectroscopy) in the electron microprobe (WDS, JEOL JXA-8900, 15 kV). Phase identification was also performed using X-ray diffraction (XRD, Malvern Panalytical Empyrean, Bragg-Brentano geometry, Cu-K α source, 1.54184 Å, 40 kV, 45 mA).

B. Computational

1. First principles calculations

We employed all-electron density functional theory (DFT)^[41] combined with the Perdew–Burke–Ernzerhof functional^[42] exchange-correlation (PBE) high-throughput calculation of formation-energy to assess thermodynamic stability of Fe-Mn-Co based MPCAs. On a few down-selected alloy compositions, we performed free-energy and vibrational entropy calculations on energetically competing HCP and FCC phases to understand the role of entropy on phase stability. The latter was done combining DFT as implemented within the Vienna Ab-initio Simulation Package (VASP)[43,44] and the Alloy Theoretic Automated Toolkit (ATAT), a random supercell generation scheme. [45] The DFT calculations on 54 (3 \times 3 \times 3) atom random supercells are conducted with a plane-wave cutoff energy of 520 eV, ensuring energy and force convergence criteria of 10^{-8} eV and 10^{-6} eV/Å, respectively. DFT-based perturbation theory calculations, post-processed with the PHONOPY package, [46] enabled the prediction of vibrational free energies and entropies.

III. RESULTS

A. Microstructural Evolution

After isothermal annealing at 1100 °C for varying times, the samples were characterized using a range of techniques. For the reference samples consisting of 100 pct MnO₂, even after long term annealing at 1170 °C, only reduction to MnO was observed, and no metallic phase was detected.

1. Effect of annealing time

Examination in the SEM revealed that samples subjected to a reduction heat-treatment of 6 hr at 1100 °C showed partial reduction to a metallic phase. Representative microstructures of sample cross-sections are shown in Figure 1. The micrographs were acquired using back-scattered electron (BSE) contrast, hence the metallic phase, which has a higher average atomic number, exhibits brighter contrast. It can be seen that in all cases the microstructures consisted of a two-phase mixture of metallic and remnant oxide phase. It is evident that metallic inclusions are present at the surface and extend into the bulk of the sample. A degree of porosity is visible, this is particularly apparent in the case of CoFeMn (x = 0), Figure 1(a), and most likely results from the reduction in volume associated with the transformation from oxide to metal. All the micrographs depict the development of a metallic layer at the sample surface. For samples with increasing Ni content,

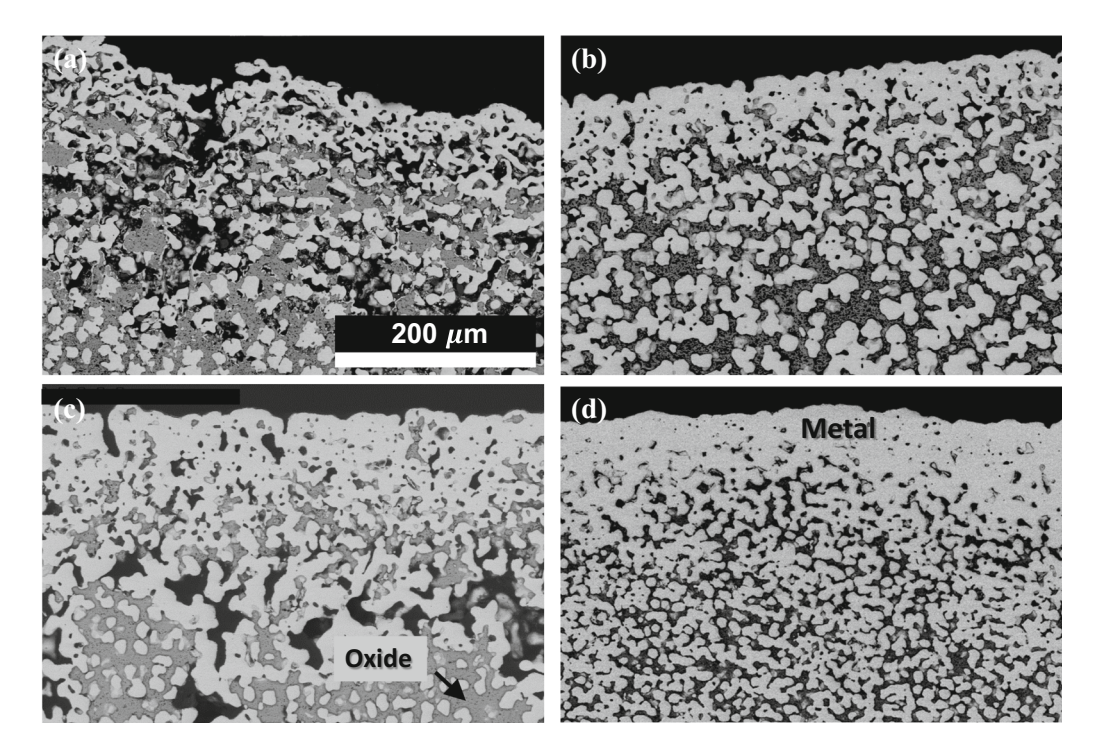


Fig. 1—Sample cross-sections after reduction heat treatment for 6 hours at 1100 °C. Microstructures show mixtures of metallic and oxide phases. (Dark contrast is porosity.) (a) (CoFeMn)_{1-x} Ni_x (x = 0), (b) (CoFeMn)_{1-x} Ni_x (x = 0.08), (c) (CoFeMn)_{1-x} Ni_x (x = 0.17), (d) (CoFeMn)_{1-x} Ni_x (x = 0.25), 10 kV, BSE contrast.

this layer becomes more well-defined and increases in thickness.

The volume fractions of metallic and remnant oxide phases were investigated using XRD. The X-ray diffraction patterns were obtained by scanning the X-ray beam across the sample cross-sections, such that the area of the scan included the entire width of the sample. The results showed that with increasing Ni content, the volume fraction of remnant MnO decreased. Specifically, the volume fraction (pct) of MnO was 40.7, 28.9, 24.3 and 13.8 for x = 0, 0.08, 0.17 and 0.25 respectively. In each case, the metallic phase made up the balance, and no other phases were detected. These results strongly suggest that the kinetics of the reduction of MnO were enhanced by increasing the nickel content.

When the reduction heat-treatment time was increased from 6 to 24 hours, it was found that all the sample compositions developed a dense metallic "shell" at the sample surface. Compared to the observations from the 6 hours samples, we can deduce that sintering of the metallic inclusions occurred and most of the porosity was eliminated. Within the core of the sample, however, the microstructure consisted of a mixture of metallic and oxide phases. This is illustrated in Figure 2, which shows a series of EDS compositional maps obtained from the CoFeMn-Ni (x = 0.25) sample after annealing 24 hours at 1100 °C (in 3 pct H₂-Ar). The micrographs are oriented such that the outer surface of the sample is situated towards the top of the image. It can be seen that there is a gradient in the oxide content, and that the phase separating the metallic inclusions is enriched in Mn and O. This type of microstructure was generally representative of all the compositions studied.

One distinction between the different compositions, however, was respect to the magnitude of the thickness (t) of the dense metallic layer. It was found that as the Ni concentration increased, the value of t also increased. The measured values were as follows: CoFeMn $(t \sim 350 \pm 30 \ \mu \text{m}),$ CoFeMn-Ni (x = 0.08) $(t \sim 270 \pm 120 \ \mu \text{m}),$ CoFeMn-Ni (x = 0.17) $(t \sim 740 \pm 50 \ \mu \text{m})$, and CoFeMn–Ni (x = 0.25) $(t \sim 980 \pm 60 \mu m)$. For each composition, therefore, a significant degree of reduction to the metallic state was achieved; for the quaternary composition CoFeMn–Ni (x = 0.25) the thickness of the metallic layer on either side was of the order of a mm, so that the sample was practically completely transformed.

B. Compositional Analysis of Metallic Phases

For both the 6 and 24 hours annealed samples, the composition of the metallic phase was determined quantitatively using WDS (wavelength dispersive spectroscopy) in the electron microprobe. Analysis was carried out from regions within a surface layer extending less than 100 μ m of the surface. The diameter of the electron beam probe was estimated to be ~ 3 μ m. In each case, the (metallic) regions of analysis were selected at random, and the results represent the average of 10 to 15 measurements. The results are given in Tables II and III.

From Table II, it can be seen that the degree of Mn reduction is greater in the quaternary sample (x = 0.25) than the sample with zero initial Ni content. This is evident not only in the measured at. pct Mn in the metallic shell (21.5 vs 15.1 at. pct), but also when

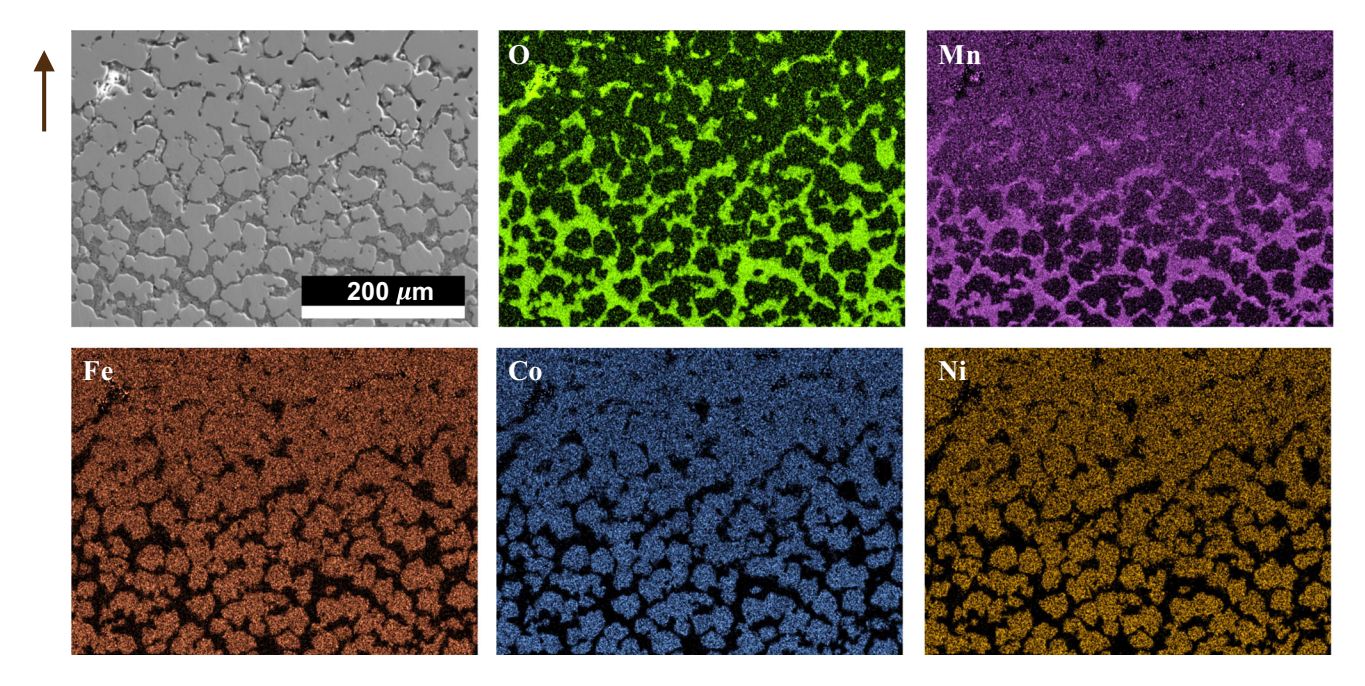


Fig. 2— $(CoFeMn)_{1-x} Ni_x$ (x = 0.25) sample annealed for 24 h at 1100 °C in 3 pct H₂–Ar. SEM (SE) image and corresponding EDS elemental maps (cross-section). (Arrow points to direction of sample surface.).

Table II. Composition of Metallic Outer Layer for Samples Annealed 6 h at 1100 °C (3 Pct H2-Ar)

Composition Wt Pct	$(FeCoMn)_{1-x}Ni_x$			
	x = 0	x = 0.08	x = 0.17	x = 0.25
Co Fe Ni Mn	53 ± 6.6 31.8 ± 3.3 N/A 15.1 ± 7	38.1 ± 1.0 27.8 ± 1.2 14.4 ± 0.6 19.6 ± 1.8	34.6 ± 1.5 25.5 ± 0.9 28.5 ± 0.9 11.5 ± 1.7	28.5 ± 1.7 19.8 ± 4.1 30.2 ± 2.7 21.5 ± 3.4

Table III. Composition of Metallic Outer Layer for Samples Annealed 24 h at 1100 °C (3 Pct H₂-Ar)

Composition Wt Pct	$(FeCoMn)_{1-x}Ni_x$				
	x = 0	x = 0.08	x = 0.17	x = 0.25	
Со	38.5 ± 2.5	32.3 ± 3.0	26.01 ± 1.7	24.6 ± 0.4	
Fe	35.04 ± 2.1	30.2 ± 3.4	28.8 ± 3.0	24.5 ± 0.3	
Ni	N/A	10.2 ± 0.9	18.5 ± 1.3	25.0 ± 0.6	
Mn	26.4 ± 1.06	27.3 ± 1.6	26.65 ± 1.46	25.8 ± 0.7	

considered as a fraction of the theoretical amount of Mn that could be achieved, 25 at pct in the case of CoFeMnNi and 33.3 at pct in the case of FeCoMn. When comparing the at. pct Fe and at. pct Co in Table II, the results show that the concentration of Co is greater than that of Fe, and that this trend persists independent of x. This finding is consistent with the thermodynamics of the reduction of these oxides, [47] in that FeO is more stable than CoO under the prevailing reduction conditions, and hence would be expected to reduce at a lower rate. Both oxides are predicted,

however, to be reducible using a dilute hydrogen mixture. This is evidenced for the 24 hour samples (Table III), where now the concentrations of Fe and Co are approximately equal, a finding that is consistent with the initial oxide powder compositions ((CoFeMn)_{1-x}-Ni_x), where the mol pct of FeO and CoO are equal, regardless of the Ni content. Another interesting result is that for the sample CoFeMn-Ni (x = 0.25), the measured concentration of the elements is very close to the targeted metallic composition, i.e. the quaternary equiatomic CoFeNiMn. What was initially somewhat

unexpected was that after annealing at 24 hour, the concentration of Mn was approximately the same for all the samples, even for the sample with zero nickel content (x = 0).

This result is considered in more detail in Figure 3, which shows the variation in Mn concentration both at the surface and within the core (depth ~ 1.5 mm) for the different sample compositions. For reference, the ideal nominal composition (assuming complete reduction of the original oxide mixture) is also included. It can be seen that in each case, the concentration of Mn in the metallic phase at the surface is higher than that in the core. This is not surprising, as the gas reduction process would be expected to initiate at the surface, and the reaction would subsequently propagate inwards. As mentioned earlier, the at pct Mn within the surface layer is practically uniform across the four compositions studied (~ 26.5 at. pct). This value corresponds closely to the theoretically expected value for the CoFeMn-Ni (x = 0.25) sample, but is somewhat less than the targeted value for the lower Ni compositions. The degree of disparity between the "ideal" and observed concentrations decreases with increasing Ni content.

C. First Principles Calculations (Including Vibrational Entropy)

First principles calculations provide additional insights on the role of the entropy driven stabilization of Fe–Co–Mn ternary compositions. Figure 4 illustrates the results from the DFT based energetics calculations. Notably, the formation energy, as determined through the KKR-CPA method, initially suggests a preference for HCP structure for the equiatomic compositions as marked in Figure 4(a) with a black star. It can be clearly observed in Figure 4(c) that the HCP phase has a lower formation energy (and is more thermodynamically stable) than the FCC phase over a temperature range

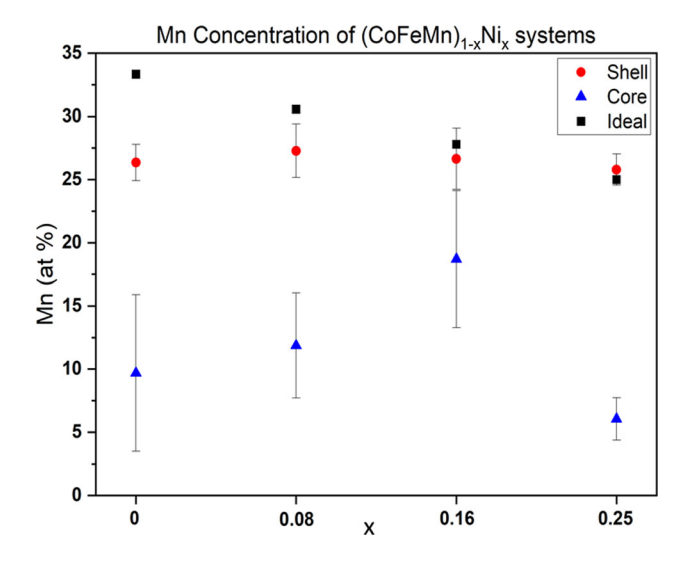


Fig. 3—Comparison of Mn concentration for the different $(CoFeMn)_{1-x}Ni_x$ samples, both at the surface and within core of sample. Ideal concentration assuming 100 pct reduction included for comparison. (annealed 24 h at 1100 °C).

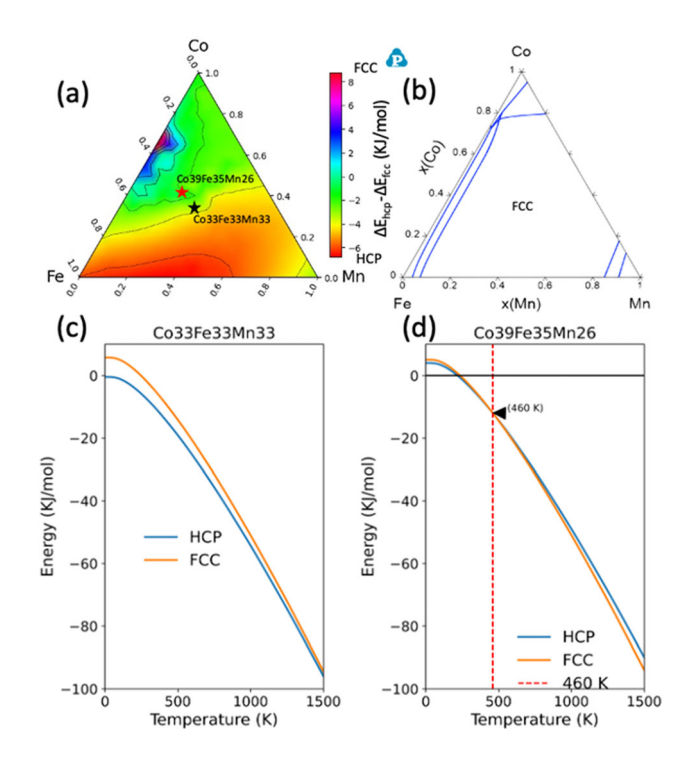


Fig. 4—Energetics calculations conducted for the CoFeMn alloy system using DFT based methods: (a) The formation energy, determined using the KKR-CPA method, where stars denote the equiatomic composition and experimental alloy composition, which serve as references for the vibrational entropy correction; (b) the phase diagram, derived from CALPHAD at 1273 K, indicates the likelihood of forming a face-centered cubic (FCC) structure within the high entropy zone; (c) and (d) showcase the vibration entropy correction for the equiatomic Co33Fe33Mn33 alloy and the non-equiatomic Co39Fe35Mn26 alloy, respectively. These plots highlight the stability of FCC over hexagonal close-packed (HCP) structures, particularly evident when compared to the equiatomic alloy in (c).

from 0 K to 1500 K for the equiatomic composition. The relative stability of the HCP phase is more heavily favored if the contribution from vibration entropy is not considered. This contradicts the experimentally observed stability of FCC phase for this composition. Additionally, the phase diagram derived from CAL-PHAD at 1273 K corroborates the dominance of FCC over HCP structures (Figure 4(b)) over a large compositional space.

For the non-equiatomic composition (marked by red star in Figures 4(a) and in (d)), the stability tendencies between HCP and FCC structures converge closely. At temperatures > 460 K, the FCC phase is slightly more favored than the HCP variant. This is the same composition that was experimentally observed in the metallic surficial layer in the CoFeMn–Ni (x=0) sample reduced for 24 hour at 1100 °C. In Figure 4(a), we found that other compositions (in light green) may also have competing phase stability, similar to experimentally observed compositions as shown in Table II. However, this needs further theoretical and experimental assessment of individual compositions. Furthermore, the observed phase discrepancy might have arisen because of the other entropic contributions such as

electronic, and magnetic entropies^[48,49] that are not considered in this study.

These results underscore the importance of entropy corrections aside from configurational entropy for understanding the phase stabilization of the MPCAs. In this work, the vibrational entropies prove crucial for juxtaposing the theoretical predictions with the experimental observations, further reinforcing the role of vibrational entropy in stabilizing the desired phase. Clearly, an intricate interplay between composition, structure, and entropy dictates the thermodynamic stability of alloys.

IV. DISCUSSION AND COMPARISON WITH PREDICTIONS OF SOLID SOLUTION MODEL

As discussed earlier, the rationale for varying the Ni content was that the binary system Ni–Mn exhibits a strongly negative enthalpy of mixing. [39,40] For reference, the essential points of the solid solution model are briefly summarized here. Using standard thermodynamic data, [50] the values of the change in free energy for the reduction of each of the component oxides $(\Delta G_{\rm red}^i)$, can be determined according to a reaction of the form:

$$\mathbf{M}_{x}\mathbf{O}_{y} + y\mathbf{H}_{2} \rightarrow x\mathbf{M} + y\mathbf{H}_{2}\mathbf{O}$$
 [1]

The total free energy change during the reaction (ΔG_{tot}) can thus be considered as follows:

$$\Delta G_{\text{tot}} = \Delta G_{\text{red}}^T + \Delta G_{\text{mix}}$$
 [2]

where $\Delta G_{\rm red}^T$ is the total free energy change associated with the reduction of all the metal oxides, and $\Delta G_{\rm mix}$ is the free energy change due to the formation of the solid solution. In turn, $\Delta G_{\rm mix}$ is given by,

$$\Delta G_{\text{mix}} = \Delta H_{\text{mix}} - T\Delta S_{\text{mix}}$$
 [3]

where $\Delta H_{\rm mix}$ and $\Delta S_{\rm mix}$ represent the enthalpy and entropy of mixing, respectively. Of these, the (configurational) entropy of mixing is readily determined from the following,

$$\Delta S_{\text{mix}} = R \Sigma_i x_i \ln x_i$$
 [4]

and the enthalpy of mixing is given by:

$$\Delta H_{\text{mix}} = 4 \sum_{(i=1, i \neq j)}^{N} \Delta H_{ij} x_i x_j$$
 [5]

where N is the number of components, ΔH_{ij} is the binary enthalpy of mixing between elements i and j, and x is the atomic fraction.

It can be seen from Eq. [2] above, that a reaction which at first sight might seem unfavorable due to a positive value of $\Delta G_{\rm red}^T$, could proceed if $\Delta G_{\rm mix}$ is sufficiently negative. These values $\Delta G_{\rm red}^T$ and $\Delta G_{\rm mix}$ were calculated at 1100 °C over the entire Co–Fe–Ni–Mn compositional range and used to determine $\Delta G_{\rm tot}$. By way of illustration, Figure 5 shows the calculated results

for ΔG_{mix} , ΔG_{red} , and ΔG_{tot} , mapped for compositions corresponding to Ni = 0.25. Note that by convention, the compositional points for a four component system can be represented by a tetrahedron with the pure elements at the vertices. For convenience the base triangle was taken to represent ternary Fe-Co-Mn compositions, hence the vertical axis represents the Ni content. Alloys with different (fixed) Ni content therefore correspond to horizontal sections parallel to the base of the tetrahedron. The variation in the free energy of mixing ΔG_{mix} (which incorporates both the enthalpy of mixing and configurational entropy terms) is depicted in Figure 5(a). As might be expected, the map shows more negative values in the central part of the figure due to the greater contribution of ΔS_{mix} . The variation in ΔG_{red}^T is shown in Figure 5(b); here the values are more negative for compositions richer in Fe and Co, but become increasingly positive as the Mn content increases. This trend clearly reflects the greater stability of MnO compared to FeO and CoO under the conditions of interest. The map of ΔG_{tot} values (Figure 5(c)) suggests that for the four component system, there is a broad range of compositions where complete reduction would be favored, *i.e.* where ΔG_{tot} is zero or negative. We will discuss the implications of this result further when considering the effect of nickel concentration on ΔG_{tot} , which is shown in Figure 6. It can be seen that for each composition, the lower region of the compositional triangle spanning the Fe-Co range exhibits value of $\Delta G_{\rm tot}$ that are zero (or negative). This implies that for these initial oxide mixtures, the complete reduction to the metallic state would be thermodynamically favorable. Note that for the original nominal compositions (x = 0 and x = 0.08) the calculated ΔG_{tot} values are positive, and indeed, these compositions were not achieved experimentally.

A comparison of the maps shown in Figures 6(a) to (d), reveals that the effect of increasing Ni addition is to (slightly) extend the region of stable compositions $(\Delta G_{\text{tot}} \leq 0)$ to higher Mn concentrations. Note that the depicted maps in Figure 6, were calculated according to the actual Ni content measured in the metallic phase, and the composition that was determined by electron microprobe is represented on the graph as a black dot. The contour corresponding to $\Delta G_{\text{tot}} = 0$ is shown as a dark line. It is worth noting that in each case, the concentration of Fe and Co are approximately equal, and that the achieved composition lies close to the boundary where ($\Delta G_{\text{tot}} \sim 0$). Specifically, the corresponding calculated total free energy change (ΔG_{tot}) for each of the four samples studied was between zero and - 10.7 kJ/mol. These results are encouraging as they are in strong agreement with the predictions of the solid solution model. The implication is that for each initial powder composition, the oxides of Fe, Co and Ni are completely reduced, whereas in the case of manganese oxide, reduction proceeds until the Mn concentration reaches the value limited by the thermodynamic consideration ($\Delta G_{\text{tot}} \sim 0$). This accounts for the disparity between the theoretical and actual Mn concentrations depicted in Figure 3. In the case of CoFeMn-Ni

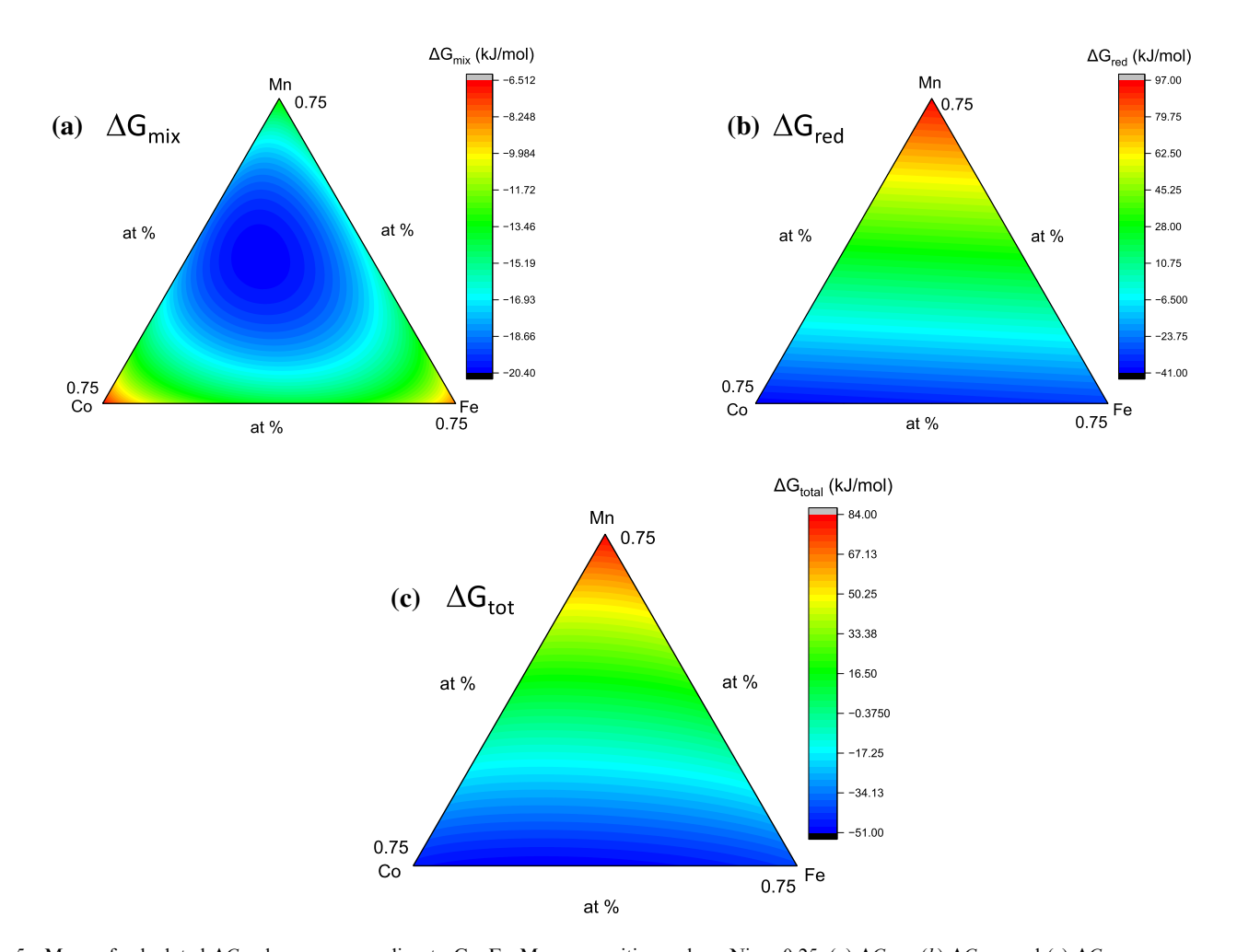


Fig. 5—Maps of calculated ΔG values corresponding to Co–Fe–Mn compositions where Ni = 0.25. (a) ΔG_{mix} , (b) ΔG_{red} , and (c) ΔG_{tot} .

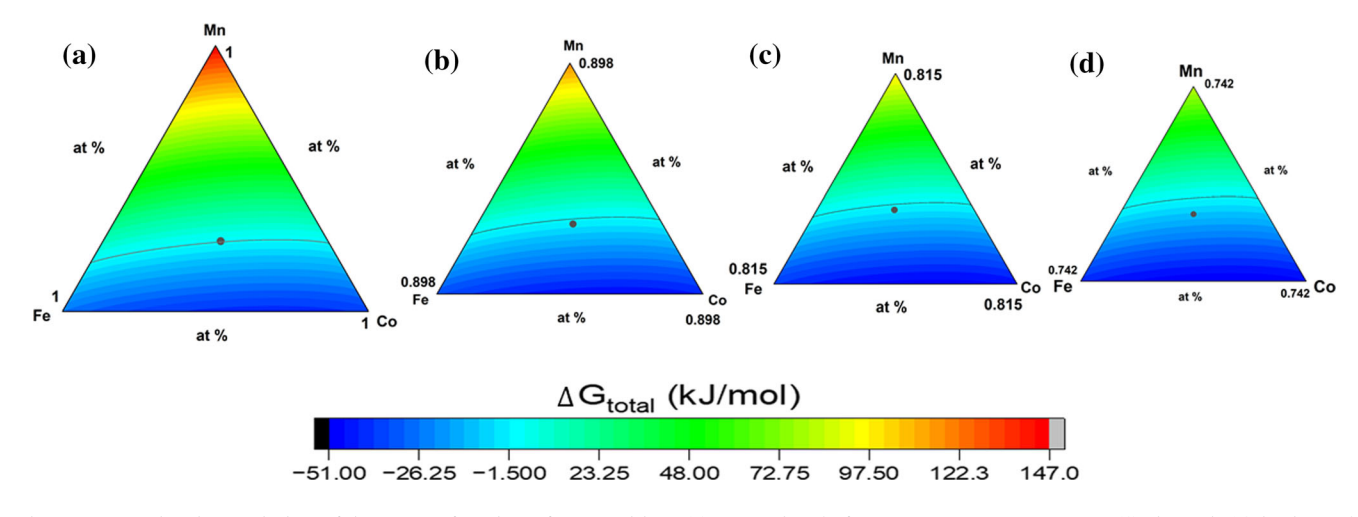


Fig. 6—Maps showing variation of ΔG_{tot} as a function of composition. (a) Base triangle for FeMnCo ternary system, (b) through (d) horizontal sections of Fe–Co–Mn–Ni compositional tetrahedron corresponding to a Ni content of 0.102, 0.185 and 0.258 respectively. The black dot represents the measured composition of the metallic phase obtained by reduction after 24 h at 1100 °C, and the line is the contour corresponding to $\Delta G_{tot} = 0$.

(x = 0), it is postulated that the substantial degree of MnO reduction was obtained due to the high negative enthalpy of mixing of Mn with Co (see Table I), so the contribution of Ni was not necessary. Another point of

interest is that for the $(FeCoMn)_{1-x}$ Ni_x (x = 0.25) sample, relative to the other specimens, the metal composition lies somewhat below the $\Delta G_{tot} = 0$ contour (Figure 6(d)). This result is consistent with the

exhaustion of MnO in the system, i.e. if more MnO had been available, a higher concentration of Mn would have been achieved! One important finding of our study, therefore, is that the mapping of ΔG_{tot} values can serve as a valuable guide as to the alloy compositions that can be achieved by the RedSSOx process.

In surveying the data, it is clear that the kinetics of the reduction process were greater with increasing Ni content. The results show that following long term (24 hour) reduction annealing, although the compositions of the metallic phase formed for the different samples were very similar, the volume fraction of metal that was obtained increased with increasing Ni concentration. It is difficult to conclude, however, whether the more rapid kinetics is the result of an enhanced driving force, or because the higher Ni content in the developing metallic phase has a positive influence on the nucleation and transport kinetics. For example, a consideration of the Ellingham diagram^[47] reveals that at 1100 °C, NiO is the most readily reduced of all the oxides present, and hence metallic Ni would be the first metal phase to form. Its presence would enhance the subsequent reduction of both Fe and Mn according to the negative enthalpy of mixing with these metals, and would hence promote the more rapid formation of a metallic phase. One might have expected the rapid formation of a dense metallic shell to act as a diffusion barrier and hence slow subsequent reduction, but this was belied by the results for CoFeMn–Ni (x = 0.25), which exhibited the highest degree of reduction. Clearly this is a complex, dynamic process, and deconvoluting these issues is the subject of future work.

V. SUMMARY

A series of oxide mixtures corresponding to the fully reduced compositions (CoFeMn)_{1-x}Ni_x (x = 0, 0.08, 0.17, 0.25) were subjected to reduction under dilute hydrogen gas conditions (3 pct H₂-Ar) at 1100 °C. It was found that in all cases, reduction heat-treatment for 24 hour at 1100 °C resulted in the formation of a dense outer layer of metallic phase that contained a significant fraction of Mn (~ 26.5 at. pct). In contrast, a sample consisting solely of MnO2 did not exhibit any reduction to metal. The study therefore demonstrated that the *RedSSOx* process can be used to successfully synthesize Co-Fe-Ni-Mn alloys containing a significant mole fraction of Mn, even under relatively benign reduction conditions. Samples with higher nickel contents exhibited more rapid reduction kinetics, so that for a given reduction time, a higher volume fraction of metallic phase was formed. A novel solid solution model was used to calculate the total free energy change corresponding to the reduction and solid solution formation of a continuous range of Fe-Co-Mn-Ni compositions. In each case, the experimental findings were consistent with the predictions of the model, in that the measured compositions of the resultant metallic phase corresponded closely to the Mn concentration at which the total free energy change was close to zero. Consideration of values of ΔG_{tot} values can therefore serve as a valuable guide as to the alloy compositions that can be achieved by the *RedSSOx* process. First principles calculations showed that vibrational entropy has a strong influence on the calculated crystal structure of the *MPCA* phase. Overall, the results of the study point to the important role of enthalpy of mixing in defining the reduction product, but more work needs to be done to fully understand the complex processes involved.

ACKNOWLEDGMENTS

The support of the NSF, Contract # DMR-2217692 (Monitored by Dr. J.D. Madison) is gratefully acknowledged. Prashant Singh acknowledges Funding support from the Laboratory Directed Research and Development (LDRD) program at Ames National Laboratory. The work at Ames National Laboratory was supported by the U.S. Department of Energy, Office of Science, Basic Energy Sciences, Materials Science and Engineering Division. Part of the research was performed at the Ames National Laboratory, which is operated for the U.S. DOE by Iowa State University under Contract DE-AC02-07CH11358.

CONFLICT OF INTEREST

On behalf of all authors, the corresponding author states that there is no conflict of interest.

REFERENCES

- B. Cantor, I.T.H. Chang, P. Knight, and A.J.B. Vincent: *Mater. Sci. Eng. A*, 2004, vol. 375, pp. 213–18.
- J.W. Yeh, S.K. Chen, S.J. Lin, J.Y. Gan, T.S. Chin, T.T. Shun, C.-H. Tsau, and S.-Y. Chang: Adv. Eng. Mater., 2004, vol. 6, pp. 299–303.
- 3. J.W. Yeh, Y.L. Chen, S.J. Lin, and S.K. Chen: *Mater. Sci. Forum*, 2007, vol. 560, pp. 1–9.
- M.-H. Tsai and J.-W. Yeh: Mater. Res. Lett., 2014, vol. 2, pp. 107–23.
- 5. F.G. Coury, K.D. Clarke, C.S. Kiminami, M.J. Kaufman, and A.J. Clarke: *Sci. Rep.*, 2018, vol. 8, p. 8600.
- 6. B. Cantor: Prog. Mater. Sci., 2021, vol. 120, p. 100754.
- D.B. Miracle and O.N. Senkov: Acta Mater., 2017, vol. 122, pp. 448–511.
- 8. B.S. Murty, J.W. Yeh, S. Ranganathan, and P.P. Bhattacharjee: *High-Entropy Alloys*, Elsevier, Amsterdam, 2019.
- M.C. Gao, J.W. Yeh, P.K. Liaw, and Y. Zhang, eds.: High-Entropy Alloys: Fundamentals and Applications, Springer, Basel, 2016.
- 10. B. Cantor: Entropy, 2014, vol. 16, pp. 4749-68.
- Y. Zhang, T.T. Zuo, Z. Tang, M.C. Gao, K. Dahmen, P.K. Liaw, and Z.P. Lu: *Prog. Mater. Sci.*, 2014, vol. 61, pp. 1–93.
- B. Gludovatz, A. Hohenwarter, D. Catoor, E.H. Chang, E.P. George, and R.O. Ritchie: *Science*, 2014, vol. 345, pp. 1153–58.
- 13. Y.Z. Tian, S.J. Sun, H.R. Lin, and Z.F. Zhang: *J. Mater. Sci. Technol.*, 2019, vol. 35, pp. 334–40.
- 14. F. Otto, A. Diouhý, C. Somsen, H. Bei, G. Eggeler, and E.P. George: *Acta Mater.*, 2013, vol. 61, pp. 5743–55.
- C. Varvenne, A. Luque, and W.A. Curtin: *Acta Mater.*, 2016, vol. 118, pp. 164–76.

- 16. O.N. Senkov, D.B. Miracle, K.J. Chaput, and J.-P. Couzinie: J. Mater. Res., 2018, vol. 33, pp. 3092–3128.

 17. S. Chen, Y. Tong, and P.K. Liaw: Entropy, 2018, vol. 20, p. 937.
- 18. Y. Chew, G.J. Bi, Z.G. Zhu, F.L. Ng, F. Weng, S.B. Liu, S.M.L. Nai, and B.Y. Lee: *Mater. Sci. Eng. A*, 2019, vol. 744, pp. 137–44.
- J. Kim, A. Wakai, and A. Moridi: J. Mater. Res., 2020, vol. 35, pp. 1963-83
- 20. B. Welk, N. Taylor, Z. Kloenne, K. Chaput, A. Kevin, S. Fox, and H.L. Fraser: Metall. Mater. Trans. A, 2021, vol. 52A, pp. 5367–80.
- 21. D. Feenstra, R. Banerjee, H.L. Fraser, A. Huang, A. Molotnikov, and N. Birbilis: Curr. Opin. Solid State Mater. Sci., 2021, vol. 25, p. 100924.
- F. Habashi, ed.: Handbook of Extractive Metallurgy, Wiley, Hoboken, 1998.
- 23. T. Rosenquist: Principles of Extractive Metallurgy, Tapir Academic Press, Trondheim, 2004.
- 24. J.H. Nadler, T.H. Sanders Jr., and R.F. Speyer: J. Mater. Res., 2003, vol. 18, pp. 1787–94.
- C. Kenel, T. Davenport, X. Li, R.N. Shah, and D.C. Dunand: Acta Mater., 2020, vol. 193, pp. 51-60.
- 26. S.K. Wilke and D.C. Dunand: J. Mater. Chem. A, 2020, vol. 8, pp.
- 27. M.J. Sharif, M. Yamauchi, S. Toh, S. Matsumura, S.I. Noro, K. Kato, M. Takatag, and T. Tsukuda: Nanoscale, 2013, vol. 5, pp. 1489-93.
- A. Verdooren, H.M. Chan, J.L. Grenestedt, M.P. Harmer, and H.S. Caram: Adv. Eng. Mater., 2004, vol. 6, pp. 397–99.
- A. Verdooren, H.M. Chan, J.L. Grenestedt, M.P. Harmer, and H.S. Caram: J. Mats. Sci., 2005, vol. 40, pp. 4333-39.
- 30. C. Kenel, N.P.M. Casati, and D.C. Dunand: Nat. Comm., 2019, vol. 10, p. 904.
- K.D. Koube, T. Sloop, C.D. Stiers, H. Sim, and J. Kacher: Additive Manuf. Lett., 2021, vol. 1, p. 100015.
- 32. M. Gianelle, A. Kundu, K.P. Anderson, A. Roy, G. Balasubramanian, and H.M. Chan: Mater. Sci. Eng. A, 2020, vol. 793, p.
- 33. M.A. Gianelle, C. Clapp, A. Kundu, and H.M. Chan: Results Mater., 2022, vol. 14, p. 100286.
- R. Kononov, O. Ostrovski, and S. Ganguly: Metall. Mater. Trans. B, 2008, vol. 39B, pp. 662-68.

- 35. S. Fritsch and A. Navrotsky: J. Am. Ceram. Soc., 1996, vol. 79, pp. 1761-68.
- 36. K.T. Jacob, A. Kumar, G. Rajitha, and Y. Waseda: High Temp. Mater. Processes (London), 2011, vol. 30, pp. 459-72.
- 37. F.E. Şeşen: J. Chem. Technol. Appl., 2017, vol. 1, pp. 1-2.
- 38. H.E. Barner and C.L. Mantell: I & EC Process Des. Dev., 1968, vol. 7, pp. 285-94.
- 39. A. Takeuchi and A. Inoue: Mater. Trans. JIM, 2000, vol. 41, pp. 1372 - 78
- 40. F.R. de Boer, FRdeWCM. Mattens, R. Boom, A.R. Miedema, and A.K. Niessen: Cohesion in Metals, North-Holland, Amsterdam, 1988.
- 41. P. Singh, A. Sharma, A.V. Smirnov, M.S. Diallo, P.K. Ray, G. Balasubramanian, and D.D. Johnson: npj Comput. Mater., 2018, vol. 4(1), p. 16.
- 42. J.P. Perdew, K. Burke, and M. Ernzerhof: Phys. Rev. Lett., 1996, vol. 77(18), pp. 3865-68.
- 43. J. Hafner: J. Comput. Chem., 2008, vol. 29, pp. 2044-78.
- 44. G. Kresse and D. Joubert: Phys. Rev. B, 1999, vol. 59, pp. 1758-75
- 45. A. Van De Walle, M. Asta, and G. Ceder: Calphad, 2002, vol. 26(4), pp. 539-53.
- 46. A. Togo and I. Tanaka: Scripta Mater., 2015, vol. 108, pp. 1-5.
- 47. O. Kubaschewski and C.B. Alcock: Metallurgical Thermochemistry, 5th ed. Pergamon, Oxford, 1979.
- 48. F. Tian, L. Delczeg, N. Chen, L.K. Varga, J. Shen, and L. Vitos: Phys. Rev. B, 2013, vol. 88, p. 085128.
- 49. P. Singh, A.V. Smirnov, A. Alam, and D.D. Johnson: Acta Mater., 2020, vol. 189, pp. 248-54.
- 50. D.R. Gaskell and D.E. Laughlin, eds.: Introduction to the Thermodynamics of Materials, 6th ed. CRC Press, Boca Raton, 2017.

Publisher's Note Springer Nature remains neutral with regard to jurisdictional claims in published maps and institutional affiliations.

Springer Nature or its licensor (e.g. a society or other partner) holds exclusive rights to this article under a publishing agreement with the author(s) or other rightsholder(s); author self-archiving of the accepted manuscript version of this article is solely governed by the terms of such publishing agreement and applicable law.